CHALMERS
UNIVERSITY OF TECHNOLOGY

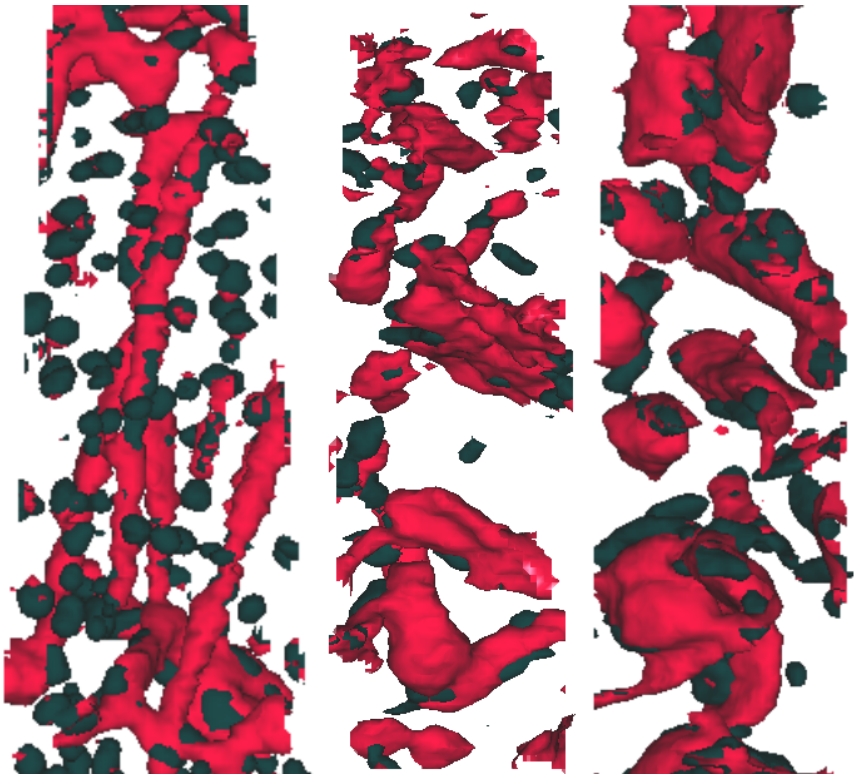

Precipitation Process in Additively Manufactured Maraging 300

An Atom Probe Study of the Precipitation Behaviour of LPBF Produced 18Ni300

Master's thesis in Physics

ERIK HERMANSSON

DEPARTMENT OF PHYSICS

CHALMERS UNIVERSITY OF TECHNOLOGY
Gothenburg, Sweden 2021
www.chalmers.se

Master's thesis 2021

Precipitation Process in Additively Manufactured Maraging 300

An Atom Probe Study of the Precipitation Behaviour of LPBF Produced 18Ni300

ERIK HERMANSSON

CHALMERS
UNIVERSITY OF TECHNOLOGY

Department of Physics
Division of Microstructure Physics
Chalmers University of Technology
Gothenburg, Sweden 2021

Precipitation Process in Additively Manufactured Maraging 300
An Atom Probe Study of the Precipitation Behaviour of LPBF Produced 18Ni300
ERIK HERMANSSON

Supervisor: Mattias Thuvander, Department of Physics
Examiner: Mattias Thuvander, Department of Physics

Master's Thesis 2021
Department of Physics
Division of Microstructure Physics
Chalmers University of Technology
SE-412 96 Gothenburg
Telephone +46 31 772 1000

Cover: Identified precipitates at 3 different stages of aging. Isosurfaces for Molybdenum (red) and titatium (dark gray) precipitates after 15, 30 and 180 minutes, respectively are shown.

Typeset in LaTeX
Printed by Chalmers Reproservice
Gothenburg, Sweden 2021

Precipitation Process in Additively Manufactured Maraging 300
An Atom Probe Study of the Precipitation Behaviour of LPBF Produced 18Ni300
ERIK HERMANSSON
Department of Physics
Chalmers University of Technology

Abstract

The precipitation process of maraging 300 steel produced with Laser Powder Bed Fusion, (LPBF), was examined using atom probe tomography. To achieve this, samples were subjected to an aging heat treatment at 500 °C for 15 min, 30 min and 180 min, in addition a sample from the as-built block was also analysed. In the as-built condition initial precipitation of $Ni_3(Ti, Mo)$ was detected together with a clustering of nickel and titanium. When aged for 15 minutes the sample showed more developed $Ni_3(Ti, Mo)$-spheres as well as $Ni_3(Mo, Ti)$-rods. There was also very slight precipitation of the Fe_7Mo_6 μ-phase at points of intersection between these rods. Upon further aging the $Ni_3(Ti, Mo)$-spheres generally decreased in size while the $Ni_3(Ti, Mo)$ formed larger precipitates of both plate- and rod-configuration. The μ-phase saw drastic increases in its size and number density upon aging for 180 minutes. It was still only found in connection with $Ni_3(Mo, Ti)$-rods, indicating that it had formed from these. At the same time there was some new $Ni_3(Ti, Mo)$-phase created as part of the $Ni_3(Mo, Ti)$-rods. This is likely a consequence of the μ-phase attracting molybdenum from the rods. As this transfer of molybdenum could start diminishing the size of the rods and the rods were at their largest at 180 minutes, it is likely the rods that contribute the most to the strength of the steel, as the 3 hour aging time is the one suggested in the literature for optimum strength.

Keywords: maraging 300, APT, precipitate, additive manufacturing, LPBF, Maraging, Age-hardening, 18Ni300.

Acknowledgements

Throughout the writing of this thesis I have learned a lot.

I would like to thank my supervisor, associate proffesor Mattias Thuvander, for his help in suggesting an interesting research topic and his expertise in the initial formulation of the problem for the thesis. In addition, we had fruitful discussions and his instruction in the usage of the atom-probe and sample preparation methods were of great help.

I would also like to extend my gratitude to Karin Frisk, our contact at Höganäs, who suggested which aging times we should analyse to help with their simulation efforts. In addition Höganäs provided the maraging 300 powder that was used to build the samples with the help of Dmitri Riabov, Chalmers. I would like to thank him for providing us with aged samples of a workable size and the adaptations made to lower the work needed to cut the sample into a small enough size.

My experimental work was performed at Chalmers Materials Analysis Laboratory (CMAL) and I would like to thank my colleagues there for their assistance with performing the sample preparation, measurements and analysis. In particular, I would like to thank Kristina Lindgren who helped with most of the atom probe measurements and with her experience had some great suggestions for a good workflow in IVAS. She was also present in the lab for most of the time and was very helpful when I had questions. Another colleague of note is Sezgin Cengiz who helped me with electropolishing of the initial batch and whose patience with my bad planning allowed me enough time at the saw to finish the sample preparation on time.

Erik Hermansson, Gothenburg, May 2021

Contents

List of Figures

List of Tables

1
Introduction

This thesis deals with the precipitation process in additively manufactured maraging 300 steel. The progression of precipitation is examined by atom probe tomography measurements at Chalmers Materials Analysis Laboratory after different times of aging at 500 °C.

1.1 Background

For many applications, high strength materials with relatively low weight are needed. One material with a rich history of usage in structural applications is steel [1]. There is however a drive towards even stronger steels as an increase in strength allows for lesser material usage and weight for a given application. At the same time optimization of the material geometry would lead to similar improvements in efficiency of use [2]. Additive manufacturing is a cost-effective way of producing intricate geometries in small production batches and during prototyping. The technique has found uses in allowing a simplification of the design process of components, creation of high strength components with intricate geometries and cheaper manufacturing of specialist parts, for example in the repair of metallic jet engine components. One of the great difficulties with additive manufacturing of steels is that common carbon bearing tool steels tend to become brittle by the extreme cooling rates of the manufacturing process. Therefore maraging steels, in particular 18Ni(300), that obtain their hardness and strength from a heat treatment process after construction are often used as they remain ductile during the manufacturing, preventing crack formation.

Maraging steels are thereby obvious contenders for use in additive manufacturing. Especially when one considers their already superior strength in bulk produced materials [3]. They have found use in aerospace and military applications, as well as in production tools such as springs, pistons and dies among many other areas of application. The strength comes from a martensitic matrix that is strengthened by intermetallic precipitates during the aging heat treatment [2]. Martensite can be formed at lower cooling rates in maraging steels because of nickel additions in the alloy mixture, allowing greater variation in processing conditions without compromising the material strength. The strengthening mechanisms of maraging steels allow higher hardness, strength and toughness without a significant decrease in ductility. In particular, precipitates hamper dislocation movement giving strength and hardness. Depending on the aging parameters used the steel will gain or lose differing amounts of strength, hardness and toughness, because of differing amounts,

types and sizes of precipitates formed. The process of precipitation during aging is therefore an important determiner of material properties of these alloys.

Knowing the precipitate properties at different times would be of great value for creating models of the precipitation process at Höganäs AB. There is currently insufficient data available for the precipitates formed in additively manufactured maraging 300 to be sure of how well the models perform and some parameters could be determined more effectively if more data were available. Knowing for instance when a given precipitate form and some of its evolution would be useful for calibration of the models. In addition, knowing how many and what sizes of the precipitates are present would be helpful in determining the probability for nucleation and the nucleation growth.

The maraging steel used in this study contain a significant amount of cobalt and nickel. The cobalt supply chain has problems with environmental impact and exploitation in the Democratic Republic of the Congo [4] and nickel mining has one of the highest environmental impacts of common metals [5]. The amounts used in this examination is however on the order of a few grams and the resulting understanding of maraging steel microstructure could lead to more efficient usage, thus the environmental and ethical costs are deemed small compared to the benefits of this thesis for the scientific community and steel component production.

1.2 Aim

The aim of the thesis is to determine type and rate of growth of precipitates in a 3D-printed maraging 300 steel. This would allow for a better understanding of the precipitation process and could lead to improvements in the modeling of the aging process.

1.3 Limitations

The thesis will be limited to a handful of samples aged for different times and at different temperatures. What happens in between these measurements can therefore only be predicted by interpolation and modeling, as well as other results from the literature. Exactly what type of crystal lattice the precipitates and bulk material have will not be determined as there is insufficient time to learn experimental techniques for this, instead these phases will be identified by comparison of atomic concentrations with literature on the subject. The process of austenitic reversion in the steel is not included in the goals of the study.

1.4 Specification of issue under investigation

What precipitates are present in the different time and temperature samples? Which geometries and sizes do they have? Do the precipitates show signs of differing growth rates in the samples? Are any of the precipitates transformed into other precipitates sometime during aging?

2

Theory

The microstructure of steel is directly linked to the mechanical properties of the macroscopic material. In this chapter some mechanisms of strengthening of steels are presented, in particular those most relevant to the maraging steel family. After this, some characterizations of the microstructure of maraging 300 found in the literature are presented followed by an introduction to the technique of atom probe tomography and how it can be used to examine the microstructure of a steel in high detail.

2.1 Strength of Steels

Although perfect crystals have very high strength in theory, pure crystals examined with experiments are often very soft and malleable [6, ch.21]. The leading cause is the dislocation, a mismatch in the lattice that follows a one-dimensional path. This type of defect can significantly ease the movement of the atomic planes. If the dislocation encounters something in the lattice that hinders its movement, some of the lost strength is regained. This can for example be in the form of a second dislocation, a grain boundary or a phase interface.

Many steels get their strength from such defects in the crystal lattice. One form this can take is interstitial or substitutional atoms increasing the strain of the lattice and hindering the shearing of atomic layers. A high dislocation density also, counterintuitively, leads to a high hardness of the steel. As many dislocations intertwine and hinder each other, the dislocations start hindering each other more than they ease the movement of the lattice planes. It is from a high dislocation density most martensitic steels derive a majority of their strength.

Martensitic steels are named for their crystal structure, martensite; a supersaturated BCC lattice formed when FCC austenite with solutes is cooled quickly enough that diffusion processes are too slow to form the equilibrium composition [7, ch.6]. The quick cooling and high solute content puts high strain on the rapidly transforming lattice, allowing for many dislocations to form. Most common steels attain this structure through carbon additions, but in maraging steels it is instead nickel that forces the martensite transition.

In maraging steels it is not only the high dislocation density of martensite that gives strength. It is also gained from precipitates formed during a heat treatment process known as aging [8]. In fact these precipitates provide most of the strength in properly aged maraging steels.

2.2 Precipitates

Precipitates consist of different phases that falls out of solution in the steel. The sizes and type of precipitates determine their hampering of the movement of defects in the lattice [1]. Most commonly the dislocations can move past precipitates with two distinct mechanisms. The first is the dislocation shearing through the precipitate. For this to happen the precipitate has to have a good match with the lattice and the energy required cannot be too large. Because the energy is proportional to the particle size, there is a size of precipitate where this mechanism stop dislocations encountered completely. For precipitates that cannot be sheared through, the dislocations instead have to bend and leave behind dislocation loops around the precipitates. This is called the Orowan mechanism and is in general weaker than the shear mechanism, as it allows the dislocations to pass by. It tends to dominate where the particles are large and reduced in numbers. Therefore there is a point at which increasing particle size becomes detrimental for dislocation movement. Large precipitates can also cause the material to become brittle depending on their type and interaction with the bulk lattice. The precipitates thus increase strength and toughness initially, but if they grow too large or a detrimental type of precipitate start growing the strengthening they provide is lessened and thus size of the precipitates must be controlled for a superior steel.

How the particles grow is a complex topic that depends on, among other things, what phase the precipitate is, how it interfaces with the bulk lattice, how easily they nucleate and concentration profiles in the steel driving diffusion [7, ch.5]. To begin with, the particles need to nucleate. This means forming a large enough particle that its interfacial energy is low compared to the energy gained from forming the new phase. This could in theory happen because of random fluctuations in the composition pushing over the critical radius of formation, but in practice it is almost always caused by some other feature that decreases the required nucleus size. For example vacancies, dislocations, grain boundaries and stacking faults increase the free energy of the lattice. Therefore nucleation of a particle that destroys such a feature may decrease the lattice energy, greatly lowering the energy barrier of the particles formation. Once a nucleus has formed, diffusion of solute elements within the matrix can cause them to grow.

The growth profile of precipitates is determined by how they interface with the bulk [7, ch.5]. For example, a particle with one plane matching the bulk lattice will tend to grow faster along the plane, producing a disc or plate-like precipitate. The growth of precipitates is therefore taking place at different rates in different directions. For spherical precipitates the radius x is proportional to the time t and diffusion coefficient D according to

$$x \propto \sqrt{Dt}, \tag{2.1}$$

as long as the precipitates are separated enough. They thicken more slowly when their diffusion fields overlap and they compete for solute elements. For the lengthening of plates and needles the relation is instead $x \propto Dt$ for any given plate thickness. This relation was derived assuming high accommodation factors which is generally not the case for broad precipitates.

The precipitates may form in several distinct phases, where phases with smaller differences from the bulk lattice is formed first followed by the precipitation of a more stable phase that grows at the expense of the first phase [7, ch.5]. In this way metastable phases may be formed and subsequently "eaten" during the heat treatment process. A similar effect is when larger particles of a precipitate is grown at the expense of smaller ones. If volume diffusion is the limiting factor the mean radius $\bar{r}$ of the particles grows according to

$$\bar{r}^3 - r_0^3 = kt, \tag{2.2}$$

where r_0 is the radius at time $t = 0$ and k is dependent on the diffusion coefficient, interfacial energy and the equilibrium solubility. As the latter increases exponentially with temperature this growth is highly sensitive to temperature variations.

As some formed precipitates are lost to larger ones this decreases another important property of the precipitates, namely their number density. With many smaller precipitates the strength increase is dominated by the shear mechanism [7, ch.5]. As more aging starts limiting the number of particles and grows their size the Orowan mechanism takes over. A high amount of smaller particles also largely lack the detrimental effects of embrittlement that come with larger precipitates. There is also a possibility for different precipitate phases to interact in a way that increases strength more than the precipitates would do on their own, producing cross terms in the determination of the steel properties.

2.3 Maraging 300

The precipitate formation in maraging steels is done via an aging process where the metal is subjected to a specific temperature for some amount of time. This precipitation hardening is the main mode of hardening for the maraging steels [9]. The time taken and temperature used determines how the precipitates form and to what extent, determining the properties of the alloy. Therefore the properties of the precipitates and their growth are of great interest [8]. The composition of the maraging 300 steel produced by Höganäs is listed in table 2.1.

Table 2.1: The composition of maraging 300 steel as listed in the datasheet [10], and converted to atomic percentages.

Conc.	Ni	Co	Mo	Ti	Al	C	Mn	Si	Fe
wt.%	18	9	5	0.7	0.1	0.01	0.1	0.1	Balance
at.%	18	9	3	0.8	0.2	0.05	0.1	0.2	Balance

Although the matrix in conventionally produced maraging steel is fully martensitic before the heat treatment, the same is not generally true for additively manufactured steel [2]. In Laser Powder Bed Fusion (LPBF) manufacturing, a laser is used to melt specific regions of a bed of metal powder. The LPBF is done in an inert atmosphere and the laser only melts a small volume of the sample, allowing for a higher heat flux. The resulting intense heating and extremely quick cooling allows a small portion of the austenite to be retained. This retained austenite can

often be found in dendritic structures of micrometer size in the martensite matrix. This austenite softens the additively manufactured steel, but the quick heating of relatively small volumes also create an altered grain structure in the martensite matrix. The high cooling rate makes the martensite formation start at more regions, allowing for a much finer microstructure with many grain orientations increasing the strength and hardness of the matrix. Thus the process of additive manufacturing both produce advantageous and detrimental effects in the steel.

How additive manufacturing techniques affect the microstructure and precipitation behavior has been studied for some combinations of aging times and production parameters [11, 12]. Austenite reversion and parameter optimization for the additive manufacturing has been of special interest in some studies [9, 13–15]. The austenite reversion is caused by nickel stabilizing austenite and is one of the processes that depend on aging parameters [8]. The precipitate formation during aging has also been of interest in recent studies [11, 12, 16]. The phases of precipitations found in these studies tend to agree with studies performed on conventionally produced material, but there are many variations of similar phases as candidates.

Precipitates described for 18Ni(300) in the literature include: a nickel rich rod- or plate-like phase variously referred to as $Ni_3(Ti, Mo)$ [2, 3, 11, 12], Ni_3Mo [13, 16] or Ni_3Ti [13, 16], a molybdenum rich phase, with several different variations reported as μ-Fe_7Mo_6 [2, 11–13], Fe_2Mo [3, 13, 16], and σ-FeMo [13], and spherical oxide particles of TiO_2 [11]. There is also a $Ni(Mo, Ti)$ phase reported in a recent study by Zhu *et al.* [17].

There are reports of two different variations of $Ni_3(Ti, Mo)$ reported in the same sample, namely a spherical and a plate-like [11], the platelike was however more molybdenum rich and attributed as $Ni_3(Mo, Ti)$ by Jägle *et al.* [18]. Of the precipitates described the nickel rich Ni_3X-precipitates are the ones contributing the most to the strength of the steel [3], while the molybdenum rich μ-phase causes brittleness in the over-aged condition. One study, [12], suggested that the precipitation starts with small Ni_3Ti-precipitates that reject cobalt and subsequently attract molybdenum. The molybdenum rich μ-phase then forms from these molybdenum enriched precipitates at the interface between the matrix and the precipitates.

2.4 Atom Probe Tomography

Atom probe tomography is an experimental technique that uses a strong electric field and a pulsed energy source to field evaporate atoms from a specimen [19, sect. 3.1]. The evaporated ions travel in the field to a detector where their position and time taken from the evaporation pulse is recorded. The detected ions can then be put into a 3-dimensional coordinate grid with a reconstruction procedure based on their hit-position on the detector and the sequence of detected ions. A thing to note is that not all ions evaporated are detected, in a Cameca LEAP 3000X HR about 37 % to 40 % of ions encountering the detector are actually detected [19, ch. 7.3.1]. From the time-of-flight data the type of ion can be deduced as the ions are separated, to a good approximation, by their mass m and charge states n through the relation

$$m/n = 2eV \left(t/l\right)^2 ,$$

where V is the applied voltage, e the elementary charge, t is the flight time and l is the flight path length [20, sect. 1.3.1]. An example of a mass spectrum from all detected ions in an analysis is shown in fig. 2.1.

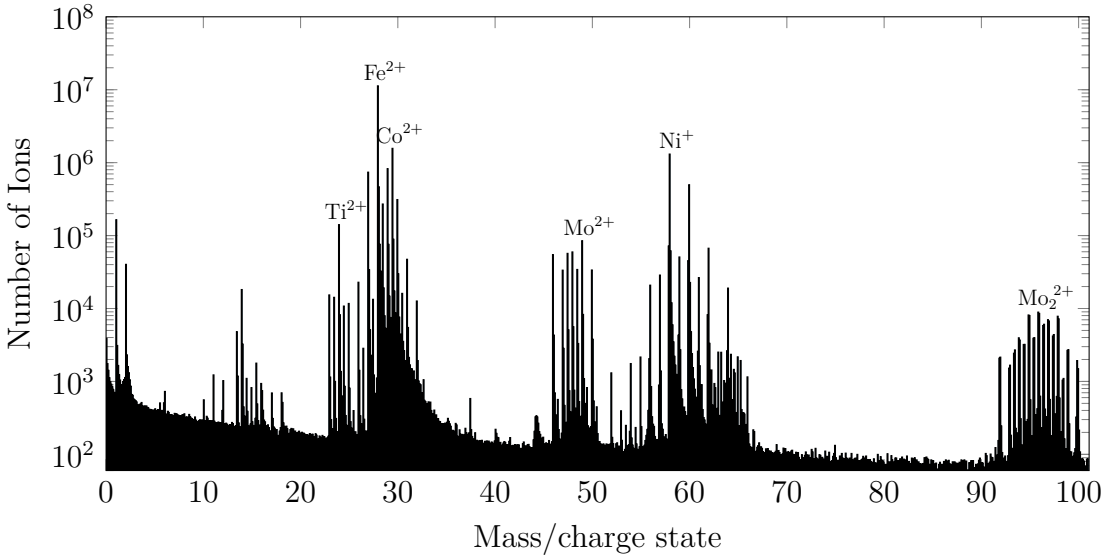

Figure 2.1: Illustration of a typical mass spectrum for bulk maraging 300. The highest peaks for all major constituents are labeled. Many of the elements such as the titanium and molybdenum were identified from their natural isotopic abundances.

The specimen is typically a very sharp needle with a roughly conical cross section and a spherical tip with a diameter initially around 20 nm to 50 nm, allowing the local field at the tip to be high enough to be close to the ionization threshold of the atoms [20, ch. 4]. This field comes from a constant applied voltage, typically in the range of 2 kV to 10 kV depending on the tip geometry and desired evaporation rate. As the evaporation rate is related to the size of the specimen tip, the voltage has to be increased as the experiment progresses to keep it high enough. An evaporation rate of up to a percent per pulse is preferred for ease of analysing the data and minimization of aberrations as a higher evaporation rate increases the risk of several ions hitting the detector at the same time registering as a single event.

To push the atoms across the energy barrier for evaporation a pulsed energy source is used. The pulses can be in the form of thermal energy from a laser or an increase in the applied field [19, sect. 3.2] as illustrated in fig. 2.2. The number and location of atoms that ionize is a function of the local field distribution at the tip and its temperature [20, sect. 3.2.4]. Appropriate temperature baselines for many metallic materials are 20 K to 50 K [20, sect. 1.3.4]. In laser pulsing mode the temperature at the surface of the tip temporarily increases, allowing for a momentarily higher thermally induced evaporation rate [19, sect. 3.2.4]. The thermal fluctuations in the sample are thus highly involved in the field evaporation process, both in voltage pulsing but especially in laser pulsing.

The temperature induced lattice vibrations together with pulse length also pose challenges, as the position of the atom at the time of evaporation and the probabilistic evaporation time after the pulse give them a spread in the time of flight spectrum

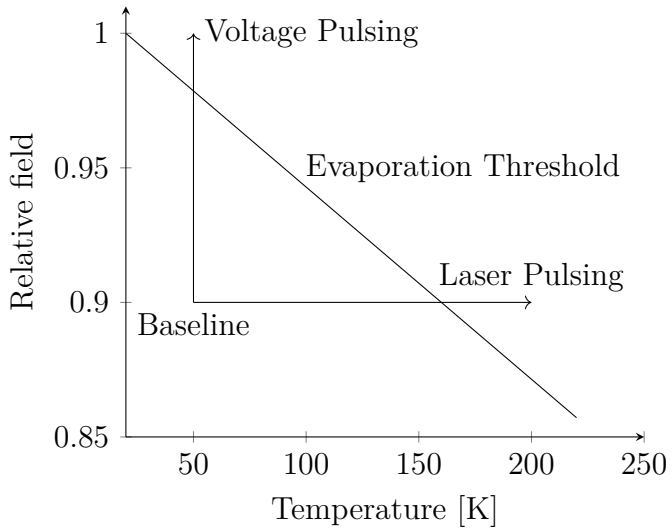

Figure 2.2: Illustration of pulsing strategies pushing the field or the temperature above the evaporation threshold.

[19, sect. 2.2]. This spread can give a mass-peak a tail long enough to overlap with other mass peaks, sometimes even obscuring them. An example is shown in the spectrum in fig. 2.3a, where several ions' tails significantly increase the background around the 31 peak. This inevitably leads to a decrease in the resolution of the data. Both in determining which ion corresponds to which element and in determining the atomic composition of data with such tails.

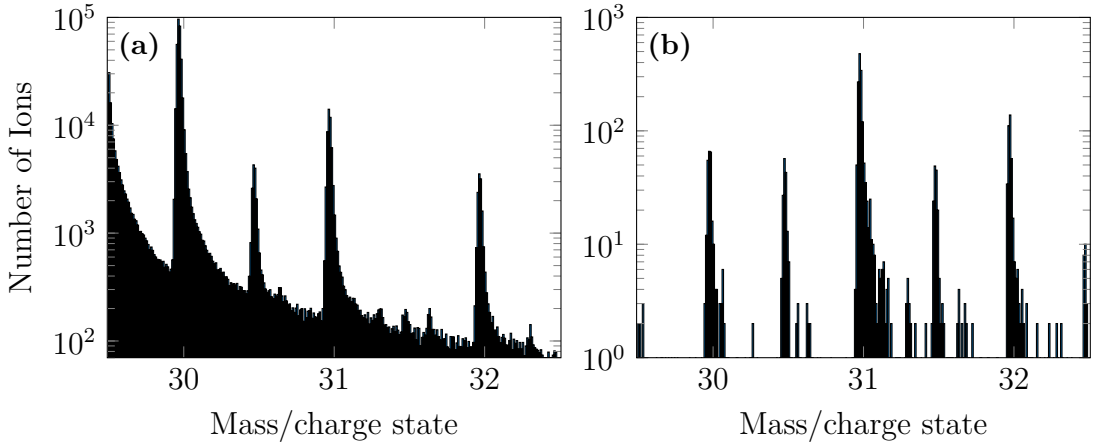

Figure 2.3: Mass spectrum for a bulk analysis (a) and the mass spectrum from a nitride particle that is a subset the same analysis (b). In the bulk the 31-peak is mostly Ni^{2+}, while in the nitride it is mainly TiN^{2+}. This is evident from the peaks surrounding the 31-peak having ratios near the isotopic abundance of titanium, nitrogen has one major peak and thus does not change the abundances much.

Another challenge in determining the atomic composition of a given data set is the fact that some ions can have the same mass to charge ratio [20, sect. 6.2.2]. This can be compensated for by examining the natural isotopic abundance of the elements in

the peak and comparing to other peaks of the same element, in fig. 2.3b for example, the type of ion can be deduced from the similar isotopic abundance of titanium. The peaks should correspond quite well in amplitude and thus the composition of the data set can be deconvoluted. However, a determination of which atom position in the peak belongs to which element is still not possible, thus limiting the accuracy of the reconstruction for these ions [19, sect. 8.1.2]. Most often, this ranging problem is handled by ranging the peak as the most abundant of the elements present and keeping these peaks in mind when analysing the data.

In addition to causing thermal fluctuations that limit time of flight accuracy, the temperature of the sample also plays a role in determining mobility of surface atoms [19, sect. 3.1.2.]. Especially for higher temperatures some elements may travel in the strong local electric fields of the surface of the specimen to zones where the field is the highest, making their position in the reconstruction inaccurate to the original sample [19, sect. 7.4]. This higher field could be at a crystallographic pole or some form of locally more curved part of the specimen surface. The higher curvature could be caused by, for instance, a precipitate that requires a higher field to have its atoms evaporated, thus leaving these atoms on a small bulge around which more easily evaporated atoms are removed first. This curvature is a significant problem as the magnification of the instrument depends on the specimen curvature [20, sect. 1.1.7]. Thus, the atoms of high field precipitates spread out more on the detector than the surrounding bulk, leaving an area of lower density in the reconstruction where the precipitate was.

Reconstruction of a sample with many different solute atoms with varying evaporation fields and precipitates therefore pose a great challenge [20, sect. 6.4]. The conventionally used algorithms for reconstruction makes some assumptions that necessarily do not hold completely true for samples with different-field precipitates. Among these assumptions are that the sample has a perfect geometry and field evaporates in a sequence closely matching the highest field [19, sect. 3.1]. In addition it is often assumed that the specimen diameter directly follows the voltage curve and can be determined from the voltage history. The many assumptions may seem damning, but the nature of the measurement process tends to smooth out the sample surface, making the assumptions more accurate. Despite the many assumptions there are still some parameters that have to be determined by the operator, but if this is done with care, sub-nanometer resolution is readily available. Examinations of the resolution has shown resolutions near 0.2 nm in the xy-plane and resolutions below 0.04 nm in the z-direction [19, sect. 8.2.1.2]. The technique thus allows for the examination of elemental distributions in 3 dimensions on a near atomic scale.

From the elemental maps of the reconstruction several features of the microstructure are directly quantifiable [20, sect. 1.3.5]. In the reconstruction, precipitates can be determined from the atomic density near them, or elemental composition, as most precipitates have differing composition when compared to the bulk material. The sizes and number of precipitates within a given volume can then be discerned [20, sect. 7.3.3], allowing one to estimate the average parameters of these. Care must however be taken as the local magnification, difficulties in determining the exact border of precipitates and how well representative the volume is for the sample can greatly affect the accuracy of the analysis. In addition to these features, grain

boundaries can often be seen if present, especially when they have been enriched by some element [20, sect. 1.3.5].

Another important tool is elemental concentration analysis of the mass spectrum from a given feature. This allows for a accurate determination of the elemental composition of the feature [19, sect. 9.1], giving clues to what phase the feature might be, and what forces drove its creation. It can also give information about rejection of solute elements from the bulk into precipitates or give an indication of early stages of clustering, a possible precursor to precipitate formation.

3
Methods

The precipitation process was examined through Atom Probe Tomography measurements at the LEAP in CMAL for samples aged at 500 °C for 15 min, 30 min and 180 min. The as-built condition, without applied heat treatment, was also examined to determine if any precipitation had already started from the LPBF manufacturing.

3.1 Sample preparation

Samples were prepared by IMS at Chalmers from powder feedstock provided by Höganäs AB. The samples were cut from a large bar of material produced using the laser powder bed fusion technique and subsequently aged in an argon atmosphere for the different times. Once the aging time was reached, the samples were water quenched to stop the precipitation growth. The heat treated samples were delivered to CMAL for the finishing stages of sample preparation.

The samples were cut into plates with a 15 HC diamond cutting blade with a Buehler ISOmet low speed saw. They were then sanded to a thickness of roughly 0.3 mm to 0.35 mm. These thin plates were then cut into roughtly square rods with dimensions of about 0.3 mm × 0.3 mm × 15 mm using the saw. The burr on the rods were cut off with a scalpel and the rods were examined in a microscope for suitability. Mainly determined by the smoothness of the surface and a square cross section.

Suitable sample rods were electropolished in a two-step electropolishing procedure illustrated in fig. 3.1. Rods were elected based on visual examination, in batches until 3-4 specimen tips had been prepared. First the rods were put into aluminium holders that were clamped to the positive electrode with a crocodile clamp. The positive electrode was held at a higher voltage compared with the platinum counter electrode allowing the acid in the electrolyte to relatively quickly etch away material. First the sample rods were necked using a 10 % perchloride solution, in 70 % methanol and 20 % glycerin, floating on Galden®. During this stage an applied voltage of 15 V to 16 V was used. In the procedure, the rod is moved up and down through the perchloride to create a tapered neck near the middle of the rod. This necking was done until the thinnest part of the sample was barely visible to the naked eye.

In the second step the necked sample rods were submerged in a 2 % perchloride solution in 2-butoxyethanol and subjected to 17 V until the top and bottom halves were separated. The needle attached to the electrode was carefully cleaned with ethanol and dried with pressurized nitrogen. The bottom needle was fished out of the percloride solution, cleaned and put in an aluminium holder. Following this,

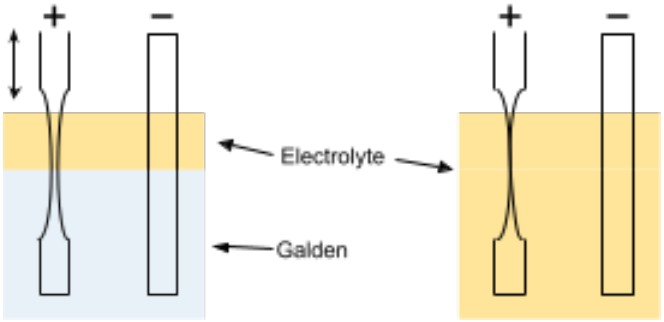

Figure 3.1: Schematic of the 2-step electropolishing procedure with step one on the left and step two on the right. In the first step the sample rod is necked by moving it up and down through an electrolyte etching away material. In the second, the necked sample is submerged in a gentler electrolyte until the bottom part of the sample breaks off.

the specimen tips were examined in an optical microscope. The best specimens in a batch were then chosen. Examples of detracting factors for this choice are visible oxidation near the tip and bent tips, these would likely cause a failure before good amounts of data could be collected. The chosen tips were then submerged in the 2 % perchloride solution and subjected to 5 short 1 ms pulses at 16 V to remove potential oxidation that had grown during the electropolishing and examination of the tips. The tips were put into sample holders and inserted into the vacuum chamber of the atom probe in preparation for the APT measurements as promptly as feasible to minimize new oxidation formation.

3.2 Atom Probe Measurements

The Atom Probe measurements were performed with an Imago LEAP 3000X HR. Measurements performed with voltage pulsing had a pulse-rate of 200 kHz and a pulse amplitude of 20 % of the base voltage. The voltage over the specimens was increased manually, while checking for alignment. The sample stage was moved to better align with the detector and the voltage was increased to show alignment from new ions. When a good voltage response of the evaporation rate was reached the instrument was set to automatically increase the voltage, aiming for an evaporation rate of 0.2 % and final adjustments of the alignment were made until the detector showed a roughly circular hit picture taking up a majority of the detector area. Data collection for all specimens were stopped after an indication of fracturing or after 70 million detection events and the data saved in RHIT-files.

With the laser-pulsed specimens a pulse energy of 0.25 nJ, a pulse rate of 200 kHz and an initial target evaporation rate of 0.2 % was used. Baseline temperatures were set at 50 K. The same procedure for aligning the sample was used, but with the extra step of also aligning the laser. This was done by a short script scanning the laser across the tip looking for the maximum of the evaporation rate and moving the laser to this position. After initial alignment this was also set to automatic control.

Once the composition of the detected ions stopped having a large fraction of

oxides, the evaporation rate was increased to 0.5 %. The reason for the lower initial rate during alignment and oxide removal is that the surface oxidation is generally weaker and a higher stress on the sample with a higher evaporation rate could cause an early fracture.

3.3 Data analysis

The data was reconstructed using the software package IVAS (version 3.6.14) in expert mode. Suitable values for the field and k-value parameters were determined through taking reasonable starting points and checking the reconstruction for signs of distortion, such as malformed precipitates, elongated precipitates growing at weird angles relative each other and inexplicable changes in specimen geometry. Once a reasonable reconstruction was found, this was used for further analysis.

The reconstructions were analysed using IVAS (versions 3.6.14 or 3.4.3) to find precipitates, clustering of atoms or other interesting features. All results presented were compiled using version 3.6.14 as it has, among other things, better background correction. Firstly, the elemental maps of the reconstructions were examined to look for denser regions of specific elements. After this, isosurfaces for elements with high density regions such as Al and O or constituents of previously reported precipitates, Ti, Mo or Ni were created. These isosurfaces were made using a voxel size of 1x1x1 nm and a delocalization of 3x3x1.5 nm. A threshold point for these isosurfaces was determined by finding were they formed nicely-shaped structures without interference from pole-lines or similar, or in the case of the more highly enriched precipitates, when they stopped being part of other precipitates. In the as-built specimens this method using atomic concentration was however insufficient. Instead, the precipitates there were found using isosurfaces for the volume density of atoms. Important to keep in mind when looking at these densities is that the detection efficiency of about 37 % makes it seem very low compared to the expected density in martensite.

Once precipitates were found, proxigrams for the interfaces of the isosurfaces were calculated. These show how the concentration of different elements changes as the interface is crossed. This is done by counting the number of atoms of a given species at different distances from the surface and examining their concentration. To improve the statistics, a proxigram for all isosurfaces of a given type were used. This leads to a lower error estimate for common sizes, but does not change the data availability within the centre of the largest precipitates, where only a few atoms are found. Examining the concentration profiles allowed identification of the concentrations corresponding to different features, both within precipitates and in the surrounding matrix. Furthermore, a new threshold point for the isosurfaces could be found by setting the concentration just below the observed precipitate composition, thus giving a more accurate representation of precipitate composition inside the isosurface, as spread of elements from local magnification effects near the edges is less pronounced.

For isolation of $Ni_3(Ti, Mo)$-precipitates, having a similar titanium concentration to $Ni_3(Mo, Ti)$-precipitates, the advanced mode of isosurface creation was useful. As the titanium to molybdenum ratio is larger than 1 for $Ni_3(Ti, Mo)$, they could be

separated in this way. The same method could also be used for μ-precipitates as the molybdenum-nickel ratio is above one for these.

The number density of precipitates was estimated from counting the number of distinct precipitates in a cutout volume of the reconstruction, deconvoluting precipitates that had grown together by the angle changes and directions of the rods in more complex precipitates. The precipitates commonly escaped this volume by the edges and a compensation for this was taken by subtracting all precipitates touching the bounds at positive x, y and z. Less intertwined regions did not need these extra steps, instead the amount at the edges was calculated from the amount of unbound isosurfaces within the volume and subsequently divided by two. The division is necessary to account for the effect of unbound particles being found on all 6 sides of the region, but on average they only make up half a precipitate each.

The volume fraction of the different precipitates was calculated by finding the number of atoms inside suitable iso-surfaces within a section of the sample and comparing with the total number of atoms inside the same section. This helps mitigate local magnification effects as the particle size in the reconstruction would look larger by the spread from the magnification. For the molybdenum rich precipitates, the number of ions inside the higher concentration μ-precipitates were subtracted from the number inside the lower concentration $\mathrm{Ni_3(Mo, Ti)}$ surface.

To determine the sizes of different precipitates they were measured by aligning boxes with their isosurface boundaries. The value of the box-width that just touched both edges of the precipitate was recorded and this was repeated for several precipitates of the same type. For a further analysis of radius distributions of roughly spherical particles, this method proved too time consuming for the large amount of precipitates in the analysis. Instead the volume, V, of bounded isosurfaces of these particles, calculated by IVAS, was used to find an equivalent spherical radius, r, for each such particle. The equivalent spherical radius is therefore given by

$$r = \sqrt[3]{3V/(4\pi)}. \tag{3.1}$$

Because of local magnification effects this overestimates the size of the precipitate. For $\mathrm{Ni_3(Ti, Mo)}$ this overestimated the size by about 10 %, when compared with the magnification corrected method. For μ-precipitates the magnification was larger, so a different way to calculate the volume was used for these. Local magnification is compensated for if one uses the number of atoms within a surface and calculates the volume they should take up in the lattice. The expression is

$$\frac{n\Omega}{\zeta}, \tag{3.2}$$

where n is the number of atoms detected in the feature, Ω the average volume per atom in the lattice and ζ the detection efficiency [20, sect. 7.2.1].

Analysis of the average atomic composition of the various precipitates was done by cutting out regions within isosurfaces with high concentration thresholds. Decomposition gives a better estimation of atomic concentration, as it compensates for background and ion overlaps, and was invaluable for the analysis of oxides. In the oxides several significant differences in composition compared with the matrix was found and many of the constituents were mislabeled using the bulk range-file. One

example is TiN^{2+} being ranged as Ni^{2+} in the peak at $m/n = 31$, as was shown in fig. 2.3.

The precipitate rod density in a 2D-plane was determined by measuring how many rods crossed a surface with a fixed area perpendicular to them. Because of the rather small area available within a sample cross section this varied a lot depending on position. Therefore only the 15 min sample was examined this way, as it had very long rods that allowed a better determination.

4

Results and discussion

The results of the analyses are presented in the order of aging time, followed by a more general discussion and summary of the results as they relate to the precipitation process. In the end some oxide and nitride particles not taking part in the aging precipitation are described and analysed.

4.1 As-built

The as-built samples were all examined with laser pulsing. The elemental maps, example shown in fig. 4.1, show no clear indication of clustering except for in large oxide or nitride particles. A lower density region through the middle of this sample looks like a very diffuse pole. This is further substantiated by it being the primary location for detected silicon as silicon tends to migrate to the poles during laser pulsing measurements. Another low density region can be found, most visible in the Co map, near the centre of the sample. This is likely caused by a small high-field precipitate that had formed.

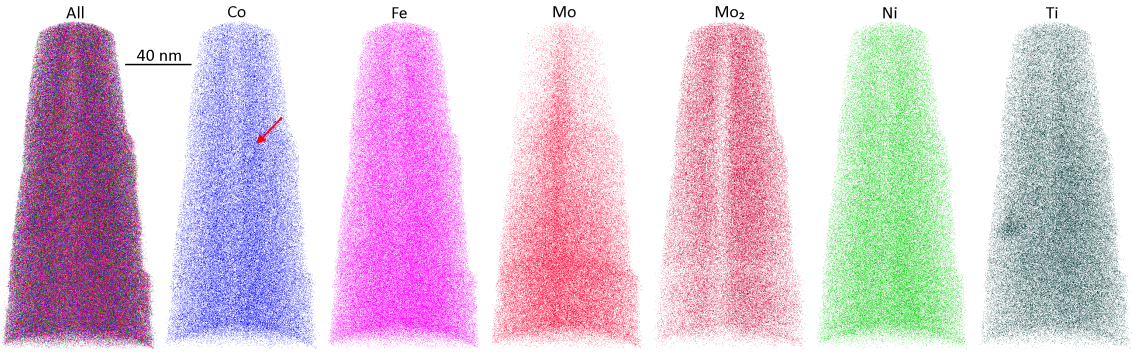

Figure 4.1: Elemental maps of an as-built reconstruction showing an enrichment of titanium at an oxide particle. Note that most elements show a lower density in the middle of the reconstruction indicating a pole. For molybdenum this region is associated with an enrichment of Mo ions and depletion of Mo_2 ions, hence there is no real depletion/enrichment of Mo. Note also a small low density circular area in the cobalt map, slightly above the centre marked by a red arrow.

In addition to this, some of the samples showed other small, low density particles in the reconstruction, as illustrated in fig. 4.2. Note that the largest such region was too close to the reconstructions edge to be included as its perimeter combined with the edge isosurface. As can be seen, these particles are not homogeneously

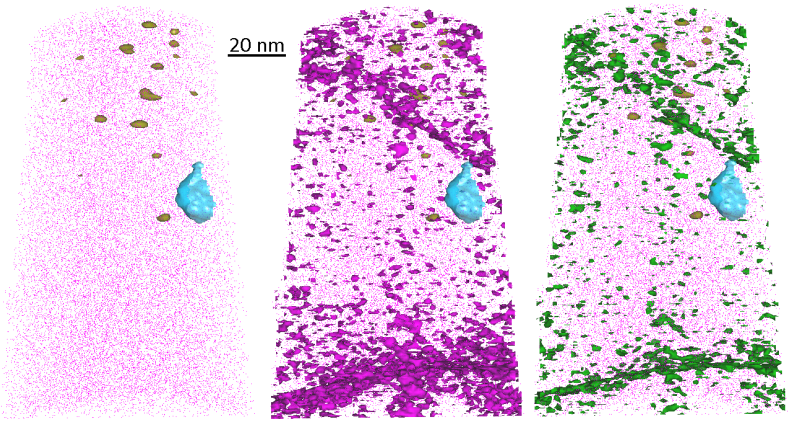

Figure 4.2: Isosurfaces for lower density particles (grey areas) in the reconstruction and a nitride (light blue) in the as-built condition, left. Isosurfaces for 71 % Fe and 15 % Ni are added in middle and right images, respectively, to illustrate likely grain boundaries.

distributed. Instead they seem to form, at least in this sample, near a grain boundary, where they have a number density of about $3.7 \times 10^{23}\,\mathrm{m}^{-3}$. An explanation could be that the likely increase of solutes near grain boundaries, together with the cyclical reheating of the laser during LPBF, leads to some "intrinsic heat treatment" nucleating precipitates. Another thing to note is the particles' very small size, the atoms within the isosurface is only about 0.1 % of all the atoms in the precipitate rich region in the top of the sample.

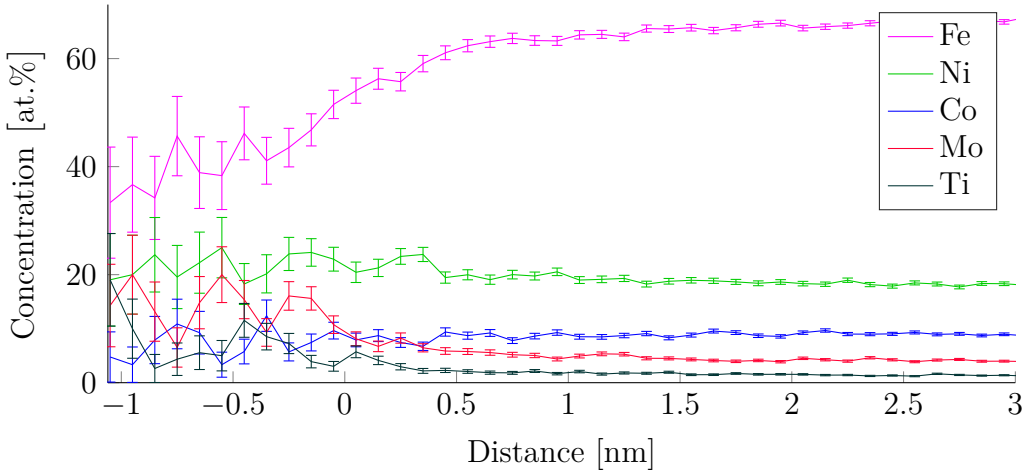

Figure 4.3: Proxigram for the lower density isosurfaces of 16.68 atoms per nm^3 in the as-built reconstruction shown in grey in fig. 4.1. Because the distance is measured with increasing density on the positive side, the particles' insides are at the negative distances. The errorbars represent the uncertainty in composition for any given distance. Note how the iron and cobalt content decreases while molybdenum and titanium increases inside the region.

To get an idea of what phase these low density particles are made of, a proxigram for the 16.68 atoms per nm^3 isosurface was calculated, fig. 4.3. The proxigram

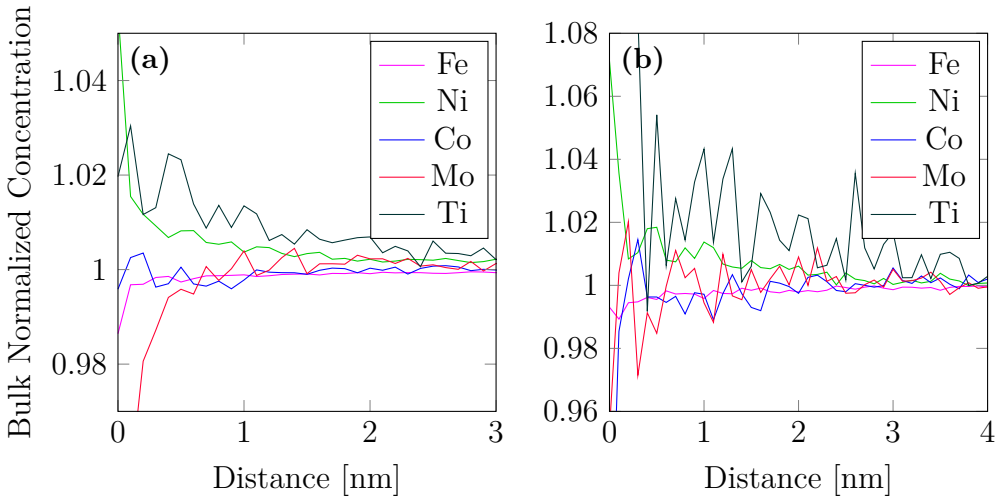

Figure 4.4: Radial distribution functions centered at (a) nickel and (b) titanium atoms in the as-built reconstruction. The average concentration of elements at specific distances from the chosen elements' reconstructed position is shown. Because there is a spread associated with atomic positions in the reconstruction it is not possible to distinguish true interatomic distances. Instead, only the tendencies of elements to be found close together is seen. Note that the volume is made small by the avoidance of poles and grain boundaries, increasing fluctuations.

clearly shows that there is a decrease of iron and cobalt in these areas while molybdenum and titanium are enriched. This would indicate that it is an early stage of $Ni_3(Mo, Ti)$ or $Ni_3(Ti, Mo)$ precipitates, even though the nickel concentration is not that high. An explanation would be that the precipitates start out as clusters of titanium or molybdenum and subsequently attract the nickel.

On closer examination of the largest such particle, the spherical region visible in the cobalt elemental map marked by a red arrow in fig. 4.1, a higher enrichment of titanium compared with molybdenum in this was noted. About $(4.7 \pm 0.1)\,\%$ Ti compared with $(6.6 \pm 0.6)\,\%$ Mo. This is an indication that the titanium rich type is the most quickly formed, which is also what is reported in the literature [12].

To get an idea about which of the elements in the sample had started clustering, a region of the sample away from the pole between the apparent grain boundaries was cut out. In this region, bulk normalized radial distribution functions (RDFs) were created for all major constituents. The resulting RDFs, fig. 4.4, show that both titanium and nickel are found slightly more often close to each other than what would be expected from the bulk, indicating the co-clustering of these elements. At the same time all major solute elements show a slight decrease of molybdenum at close distances in their respective RDFs, except the one for molybdenum. The RDF for molybdenum has a slight increase in both molybdenum and titanium in a near proximity. It could be that molybdenum with its large radius forms an early clustering in areas where it has more space in the lattice and these sites reject elements with smaller radii. As titanium also has a larger than average radius its presence does not discount this explanation. Another explanation would be that molybdenum is a more difficult element to analyse as it was present as both Mo_2

and Mo, leading to some form of artifact in the RDF.

The matrix composition was analysed in the area above the upper, below the lower and between the grain boundaries shown in fig. 4.2. The compositions, presented in table 4.1, show that the two upper regions have a higher titanium content. It was in these regions that the precipitation had started. Interesting to note is that there is no significant difference in molybdenum content between the regions, again giving an indication that titanium is the more important element for early stages of precipitation. The composition within the lower density regions show an enrichment of nickel, molybdenum and titanium, supporting the analysis that $Ni_3(Ti, Mo)$ or $Ni_3(Mo, Ti)$ are the early precipitates.

Table 4.1: Elemental composition of the matrix above the upper apparent grain boundary, between them and below the lower as well as the composition inside the low-density particles of the as-built sample shown in fig. 4.2.

Conc. at.%	Fe	Ni	Co	Mo	Ti
Matrix upper	68.2	18.1	9.16	3.81	1.15
Matrix between	68.0	18.3	9.08	3.77	1.13
Matrix lower	69.5	17.8	9.04	3.06	0.707
Particles	50.0	21.3	7.84	10.9	5.47

4.2 Aged at 500°C for 15 min

The samples aged for 15 min has a more developed microstructure. From the elemental maps, example shown in fig. 4.5, it is evident that both molybdenum and titanium has formed precipitates.

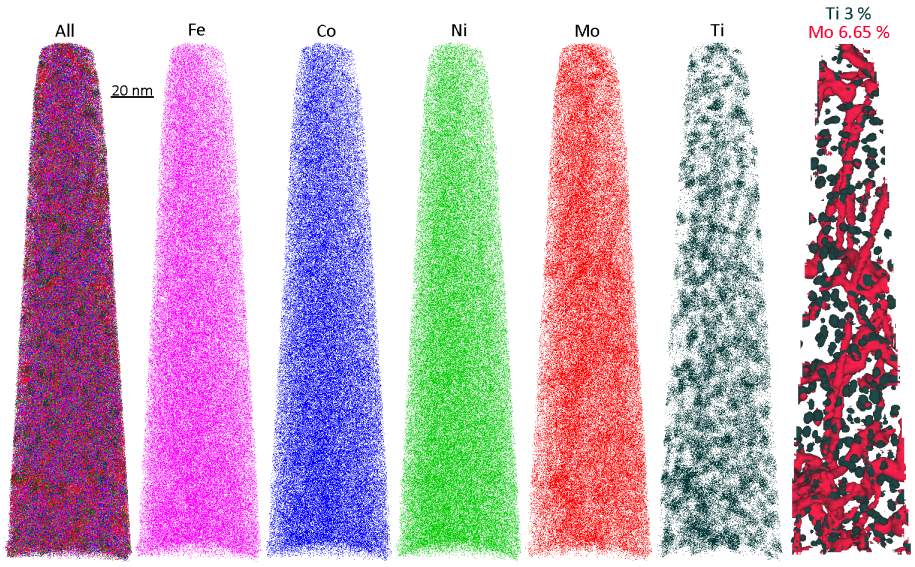

Figure 4.5: Elemental maps of the main constituents in the steel aged for 15 min. Also shown are isosurfaces for 6.65 % Mo and 3 % Ti to more clearly illustrate the precipitates.

The precipitates have formed into different shapes, with the molybdenum rich being rod-like and the titanium rich spherical. The rod-like molybdenum enriched regions have an average diameter of roughly 4 nm and lengths up to 50 nm before a slight angle change and near 100 nm overall. Because they formed preferentially aligned well along the z-axis the entire length of most precipitates could be measured. The formation of rods along very distinct axes suggest that they are coherent with a plane direction in the matrix lattice, as would be expected. The angles between rods and connections to other rods are usually 90°, but 60° angles are also present, again suggesting that they might grow coherently with the matrix as the [110] directions of a BCC lattice has these angles. In a $30\times30\times300\text{nm}^3$ region of a larger reconstruction these rods have a calculated number density of about $1.7 \times 10^{23}\,\text{m}^{-3}$, while in a precipitate-rich $35 \times 35 \times 70\text{nm}^3$ region they reach $2.7 \times 10^{23}\,\text{m}^{-3}$.

The rods are also enriched in titanium. The composition within the isosurface is illustrated in a proxigram in fig. 4.6a. The composition nears that of $Ni_3(Mo, Ti)$ reported by Jägle *et al.* [18] closer to the center, but precipitates with radius larger than 2 nm seem to head towards a less nickel and titanium rich and a more molybdenum rich composition in the core. It can also be noted that the Fe content is relatively high, suggesting that some Ni positions are occupied by Fe.

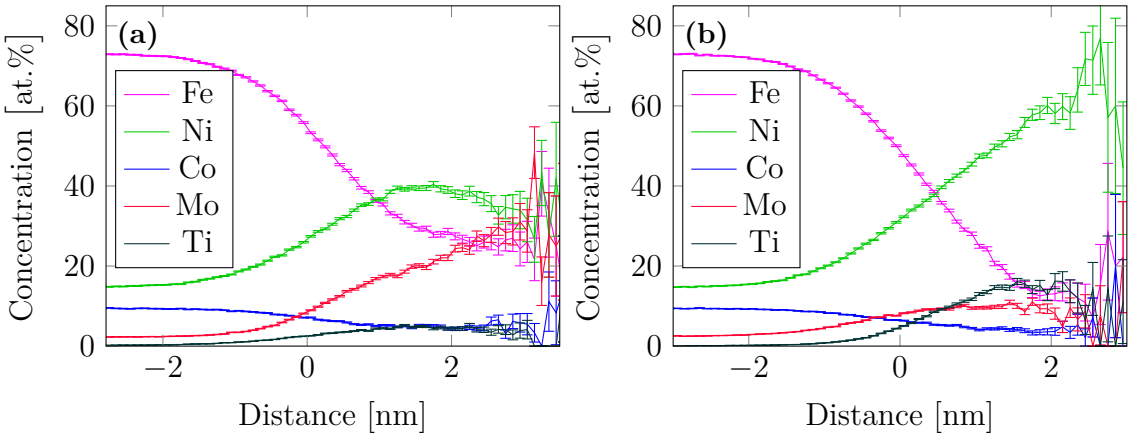

Figure 4.6: Proxigrams for (a) 6.65 % molybdenum and (b) 3 % titanium isosurfaces in the 15 min sample. The particles are on the positive side of the interface. To note is that the largest distance in (a) show a decrease in nickel. Thus, the largest precipitates likely have a different composition, at least in the middle. The proxigram in (b) show a higher concentration of molybdenum than that reported by Jägle *et al.*, but some regions of the two isosurfaces overlapped.

The titanium rich spheres, a proxigram of which is illustrated in fig. 4.6b, seem to be of the $Ni_3(Ti, Mo)$ composition that Jägle *et al.* described. The percentage of molybdenum is higher in this analysis, but some of the isosurfaces are within the molybdenum rich rod-like precipitates. To deal with these effects, isosurfaces where the titanium content is higher than molybdenum were created. These were all almost spherical, or a combination of several spheres, indicating that a distinct phase from the rods was found. The same was done with molybdenum concentration higher than nickel to find potential μ-Fe_7Mo_6 precipitates.

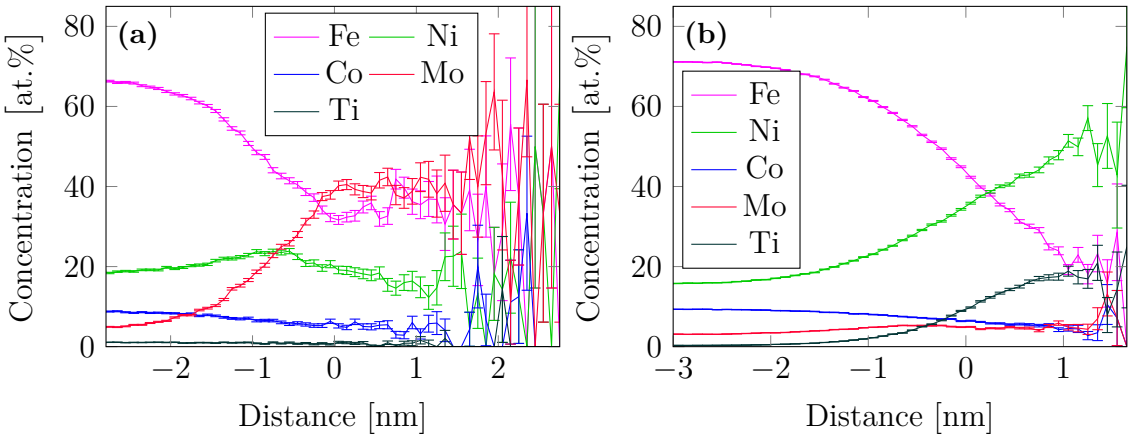

Figure 4.7: Proxigrams for (a) molybdenum greater than nickel and (b) titanium greater than molybdenum isosurfaces in the 15 min sample. This can be interpreted as isolated μ-phase and $Ni_3(Ti, Mo)$ as the concentration of elements inside the particles, positive direction, has their compositions.

The resulting proxigrams are shown in fig. 4.7. From fig. 4.7b, it is evident that already after 15 min some μ-Fe_7Mo_6 precipitates have formed. The number density of these is about $1.9 \times 10^{22}\,\mathrm{m}^{-3}$. They are found at the ends of the molybdenum rich rods, often where two or more rods connect. It could be that the μ-Fe_7Mo_6 precipitates act as sites from which the longer rods grow as Jägle *et al.* [18] suggested. Some rods do however lack such endings indicating that it is instead the rods that form first and it is from the rods the μ-phase forms.

Taking away the parts of the rods that had a μ-phase composition their volume fraction was about 1.9 %. The amount of μ-phase is significantly lower at about 0.02 %. Interestingly, the volume fraction of $Ni_3(Ti, Mo)$-spheres is a lot lower than the $Ni_3(Mo, Ti)$-rods at about 0.32 % despite their higher numbers.

The number density of titanium-rich spheres in the same $30 \times 30 \times 300\mathrm{nm}^3$ sub-volume that was used for the rods was calculated. In this volume 169 particles were found of which 111 were bounded. It thus gives a number density of $5.2 \times 10^{23}\,\mathrm{m}^{-3}$ of $Ni_3(Ti, Mo)$-particles. In the more precipitate rich region a value of $8.6 \times 10^{23}\,\mathrm{m}^{-3}$ was found. The precipitate rich region could be around a grain boundary as it is relatively flat in the xy-plane and would explain an increase in solute availability and thus precipitate formation.

As the titanium rich precipitates are near-spherical their radii can be approximately calculated from their volume by assuming they are perfect spheres. From the interfaces created by isosurfaces in IVAS, bound regions have their volume reported. From this reported volume value of the at.%Ti > at.%Mo isosurface interfaces the equivalent spherical radii were calculated and binned into a histogram, fig. 4.8. The histogram illustrates that there is a range of radii for these particles with a mode around 1.1 nm and a mean radius of 1.2 nm. One thing to note is that some particles were close enough together to touch and thus there is a slight over-reporting of larger radii.

Mass decomposition analysis, summarized in table 4.2, shows that the matrix

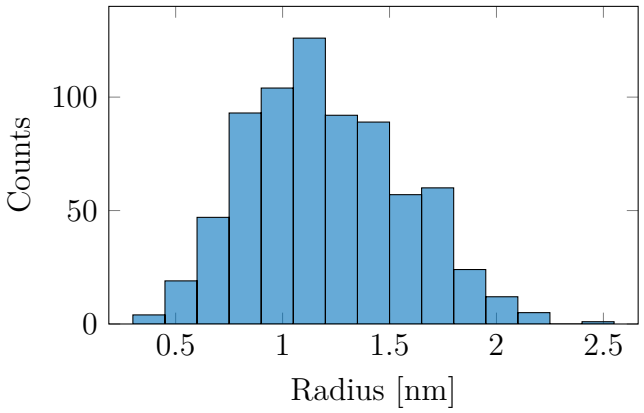

Figure 4.8: Histogram showing the abundance of particles with at.%Ti > at.%Mo by radius in the samples aged for 15 min.

is depleted in the elements of the precipitates, and therefore enriched in cobalt and iron. The $Ni_3(Ti, Mo)$ have a very enriched composition with almost no iron detected within the isosurfaces. The rods have a more significant iron content and show a relatively low molybdenum content when compared to the values reported in the literature. The μ-precipitates are relatively low in titanium but higher in cobalt when compared to the other precipitates. Interesting to note is that the molybdenum content is higher than iron despite a nominal composition with more iron. This can be explained by the substitution of iron in the μ-lattice with nickel or cobalt atoms. Another explanation for this higher detected nickel content could be that the μ-phase is attached to the more nickel rich $Ni_3(Mo, Ti)$-phase and some of the nickel atoms were placed on the wrong side of the isosurface during reconstruction.

Table 4.2: Elemental composition of the matrix and identified precipitates in the sample aged 15 min

Conc. at.%	Fe	Ni	Co	Mo	Ti
Matrix	75.5	13.3	9.23	1.71	0.119
$Ni_3(Ti, Mo)$	7.88	54.9	4.40	9.27	24.2
$Ni_3(Mo, Ti)$	36.4	40.7	5.22	12.4	5.58
μ-Fe_7Mo_6	30.1	22.5	5.75	40.2	1.16

The composition of the rod-like precipitates has very similar ratios to the rod-like $\eta - Ni_3(Ti, Al)$-phase found by Thuvander *et al.* [21] in a maraging steel. It could be the case that the detected rods have the same crystal lattice, as they are found in similar steels and have similar geometries.

4.3 Aged at 500°C for 30 min

The sample aged for 30 min fractured after a relatively small amount ions were captured for two distinct specimens. The reconstruction for one of these is shown in fig. 4.9. This shows many interesting features: the molybdenum isosurface is

found as both rods and plates while the titanium particles seem slightly elongated. Changing the reconstruction parameters does not change the plate-like precipitates into rods, because of their orientation, indicating that they are truly plates. In the

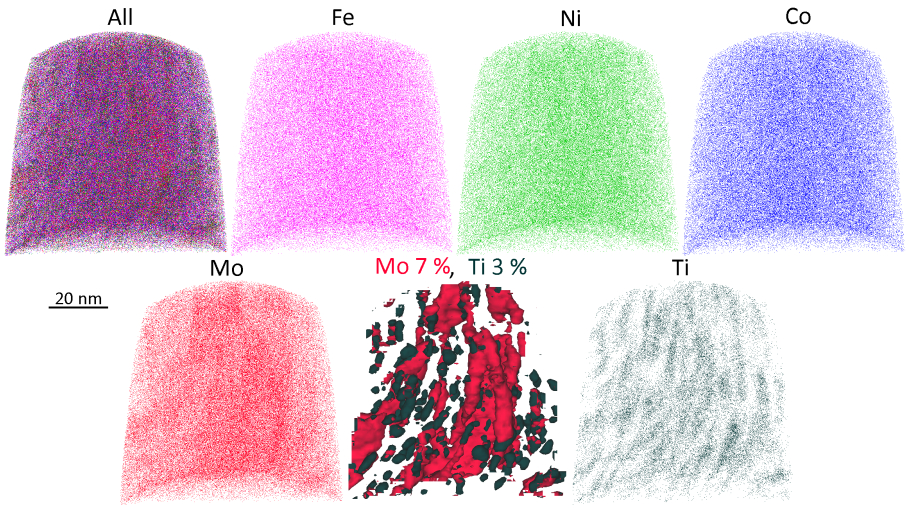

Figure 4.9: Elemental maps of the main constituents in the steel aged for 30 min. Also shown are isosurfaces for 7 % Mo and 3 % Ti to more clearly illustrate the precipitates.

reconstruction with the most reasonable appearance, the plates had a thickness of about 5 nm and a width of 15 nm, while the rods had a diameter of about 5 nm, lengths reached 50 nm before being cut off by the end of the specimen.

The other specimen showed a constitution more similar to the 15 min specimens. There was a large difference between these microstructures and the small amount of data make it difficult to establish which is more representative of the sample as a whole. In both specimens, precipitates of the $Ni_3(Ti, Mo)$ and μ-Fe_7Mo_6 types were found. Isosurfaces were calculated in the same way as for the 15 min case and their proxigrams for the second specimen are shown in fig. 4.10. It would seem like the μ precipitates are smaller when compared to the 15 min case, the examined volume is however much smaller and thus the chance of finding some of the larger precipitates, if present, is relatively smaller.

The two different specimens showed a large difference in microstructure also in the abundance of precipitates. The reconstruction shown in fig. 4.9 had a number density of $Ni_3(Ti, Mo)$-particles at $5.1 \times 10^{23}\,m^{-3}$ while the other had a number density of $1.3 \times 10^{23}\,m^{-3}$. For the μ-precipitates, the reconstrucitons only contained a couple of precipitates and only one of the volumes used contained one, giving a number density of $1.9 \times 10^{22}\,m^{-3}$. For the rod- and plate-like precipitates the number density was $5.5 \times 10^{23}\,m^{-3}$ and $2.3 \times 10^{23}\,m^{-3}$, respectively.

Despite the specimens having very different appearances and matrix composition, the sizes of $Ni_3(Ti, Mo)$ had a very similar distribution and they are combined in fig. 4.11, showing that the radii are similarly distributed as in the 15 min sample. The mean radii were 1.02 nm and 1.13 nm in the two specimens. The distribution is a bit flatter and slightly shifted towards smaller radii when compared with the 15 min case in fig. 4.8. One of the largest of these precipitates was found in between a rod

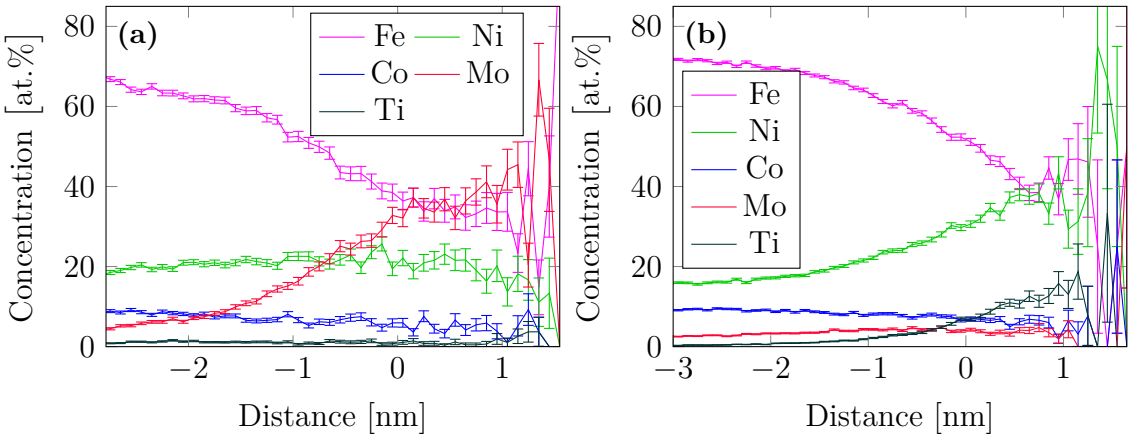

Figure 4.10: Proxigrams for (a) molybdenum greater than nickel and (b) titanium greater than molybdenum isosurfaces in the 30 min sample. This can be interpreted as isolated μ-phase and $Ni_3(Ti, Mo)$ as the concentration of elements inside the particles, positive direction, has their compositions.

and a plate. The centre of the rod was aligned with the sphere and if the rod would be extended through the sphere it would connect with the plate. Interesting to note is the composition of this particular rod. It has a much lower nickel abundance than the other rods.

Table 4.3: Elemental composition of the matrix and identified precipitates in the specimens aged 30 min. The composition of the precipitates was determined from the first specimen. Note that the two specimens had large differences in matrix composition.

Conc. at.%	Fe	Ni	Co	Mo	Ti
Matrix sp.1	73.9	14.7	9.11	2.07	0.120
Matrix sp.2	76.0	12.6	9.05	1.90	0.505
$Ni_3(Ti, Mo)$	46.3	34.6	4.45	3.67	10.4
$Ni_3(Mo, Ti)$	52.0	30.2	6.40	9.87	2.26
μ-Fe_7Mo_6	51.5	18.3	6.28	24.7	0.793
Mo-rich, Ni-poor	61.6	18.9	7.53	11.2	0.372

The composition in the identified features of the sample is summed up in table 4.3, showing also the composition in the rod without much nickel. The compositions has a higher abundance of iron when compared to reported values in the literature, but the molybdenum-titanium-nickel ratios is similar to the phases reported. The composition of the molybdenum-rich nickel-poor phase is not easily identified as a phase reported in the literature. The most similar phase, albeit for a more aged condition, is the Ni(Mo, Ti)-phase reported by Zhu *et al.* [17]. Otherwise it could easily be a metastable phase that only forms when molybdenum rich rods hit $Ni_3(Ti, Mo)$-spheres, possibly depleting them of titanium. At the same time the precipitate could be a prephase for the formation of $Ni_3(Mo, Ti)$-rods that was stunted by a $Ni_3(Ti, Mo)$-sphere.

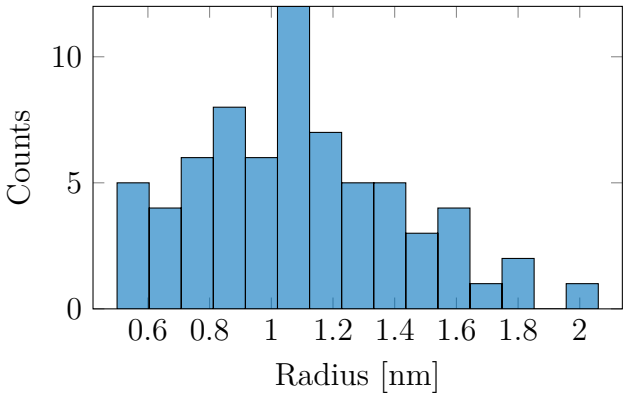

Figure 4.11: Histogram showing the abundance of particles with at.%Ti > at.%Mo by radius in the sample aged for 30 min. Note that the smaller size of the specimen reconstruction is a source of greater variance and fewer counts, when compared with the other states.

4.4 Aged at 500°C for 180 min

Several different precipitates formed in the sample aged for 180 min and their separation from the matrix is clearly visible in the elemental maps in fig. 4.12. There were precipitates highly enriched in molybdenum and different forms of precipitates rich in nickel. Long rods of $Ni_3(Mo, Ti)$ were present in the reconstructions. Most of these cut through the analysed volume through the xy-plane, but a few were closer to the analysis direction and measured around 100 nm in length before leaving at both edges.

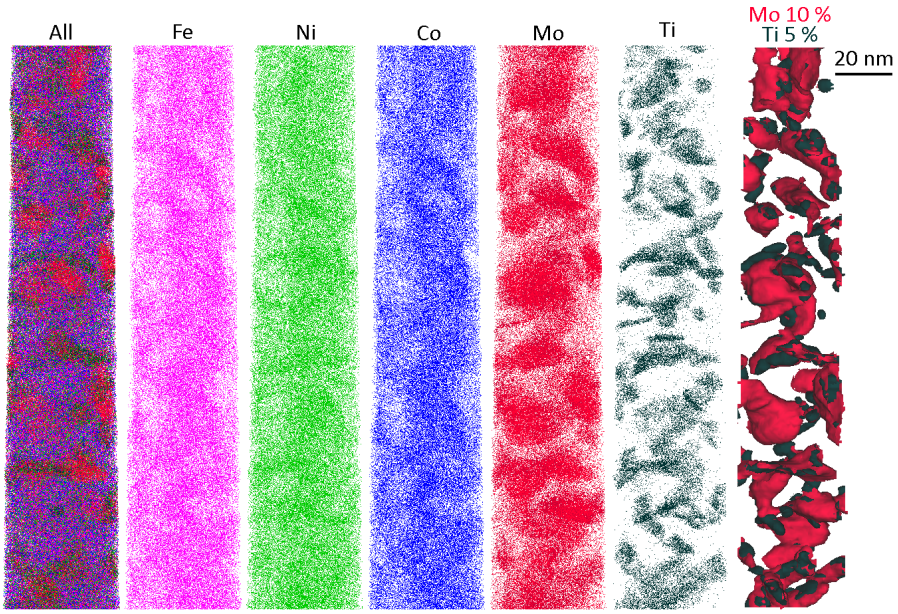

Figure 4.12: Elemental maps of the main constituents in the steel aged for 180 min. Also shown are isosurfaces for 10 % Mo and 5 % Ti to more clearly illustrate the precipitates.

The precipitates with greatly enhanced molybdenum content but depleted of nickel, shown in fig. 4.13a, were exclusively found connected to precipitates of the $Ni_3(Mo, Ti)$ type. The precipitates rich in titanium but lacking in molybdenum, proxigram showed in fig. 4.13b, were found mainly as spherical particles in solute-depleted regions of the samples. There were however some that were more rod-like, these being found attached to molybdenum-rich rods near μ-particles. They seem to follow the stoichiometry of the $Ni_3(Ti, Mo)$ phase.

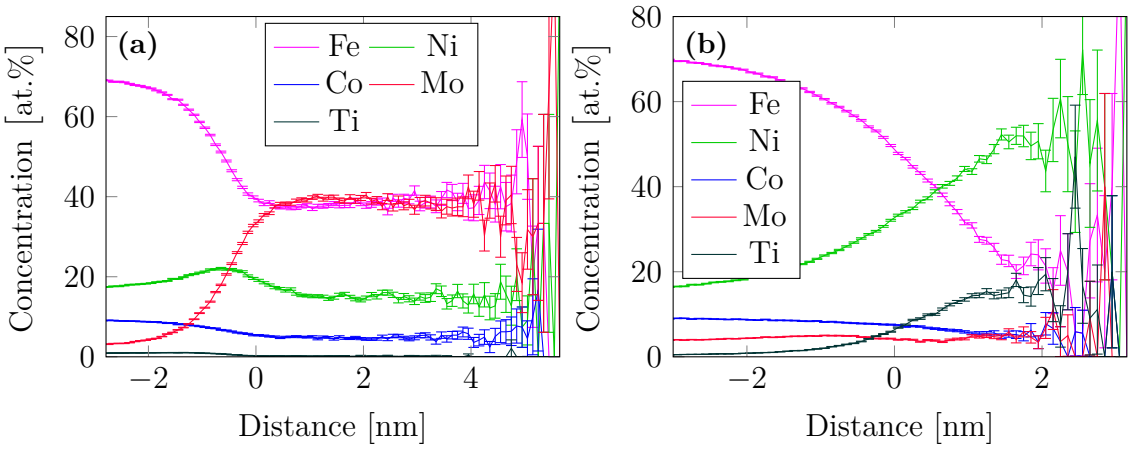

Figure 4.13: Proxigrams for (a) molybdenum greater than nickel and (b) titanium greater than molybdenum isosurfaces in the 180 min sample. This can be interpreted as isolated μ-phase and $Ni_3(Ti, Mo)$ as the concentration of elements inside the particles, positive direction, has their compositions.

Counting the number of particles of $Ni_3(Ti, Mo)$ type in a a $25 \times 25 \times 500 nm^3$ volume gives 147 particles of which 66 were bound. The number density comes out as $3.4 \times 10^{23}\,m^{-3}$, lower than in the less aged samples, but the volume fraction was higher at 0.86 %. The amount of $Ni_3(Mo, Ti)$ precipitates within the same volume was counted to be 101, of which 7 were comprised of several distinct parts estimated to be about 25 distinct precipitates that had grown together. There were 37 of the total precipitates that touched any of the 3 sides set as boundaries giving a number density of $Ni_3(Mo, Ti)$ precipitates of $2.6 \times 10^{23}\,m^{-3}$. The volume fraction was 3.6 %, the highest in all measured samples. The same calculation for the μ precipitates gave 57 precipitates of which 7 were unbounded. The number density of these is therefore given as $1.0 \times 10^{23}\,m^{-3}$. The volume fraction of these were 0.86 %.

The sizes of the precipitates were, as indicated by the volume fraction, much larger than for less aged samples. Because of the large degree of separation in phase compositions, the μ-phase could now also be detected using a 29 at.% Mo isosurface. The μ precipitates had diameters ranging from 15 nm to 25 nm in the reconstruction if defined by 29 at.% Mo and 8 at.% to 13 at.% if defined by Mo > Ni. Local magnification of the rods could cause an increase in apparent nickel content in the μ-phase making the Mo > Ni isosurface smaller than expected. The same effect with the local magnification from μ-precipitates should increase the apparent size of the 29 at.% Mo isosurface. The second makes the μ precipitates a bit larger than

the diameters of the rods, being between 10 nm to 15 nm, the other a bit smaller. The total length of the rods could not be determined as they did not align with the analysis volume.

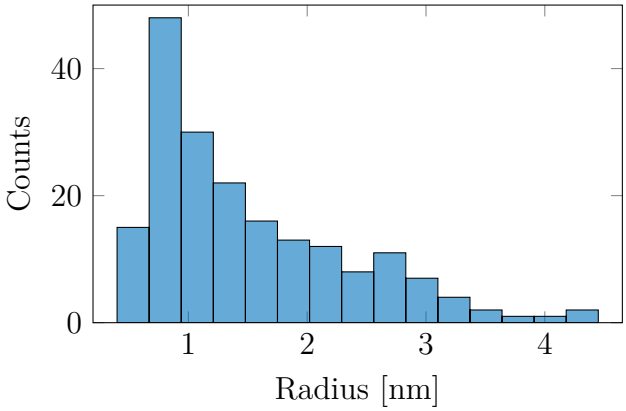

Figure 4.14: Histogram showing the abundance of particles with at.%Ti > at.%Mo by radius in the samples aged for 180 min.

The size distribution of $Ni_3(Ti, Mo)$, shown in fig. 4.14, has its mode even further shifted towards smaller particles compared to the less aged states figs. 4.8 and 4.11, but is stretched to include larger radii, leading to a mean radius of 1.51 nm. Some of these are spheres with a large radius, but others are the rods that had been depleted in molybdenum. Some shift towards higher radii is expected as the larger precipitates usually grow with time at the expense of smaller ones. The fact that very few of the spherical precipitates become larger does however indicate that the $Ni_3(Ti, Mo)$ precipitates are expended when the $Ni_3(Mo, Ti)$-phase grows, as it has a considerable portion of titanium in its lattice. The volume fraction of $Ni_3(Ti, Mo)$-particles had however grown despite the decrease in number of particles, mainly because of the rod-like parts that had started forming from the rods.

To determine the amount of solute in the matrix and precipitates a peak decomposition was made and is summarized in table 4.4. The amount of titanium and molybdenum in the matrix shows how the precipitation has almost absorbed all of the available solute compatible with the precipitates at this time. Some nickel remains in the matrix, but the precipitate compositions are near the nominal nickel levels, meaning not much of the remaining nickel could be absorbed by the precipitates. The rejection of cobalt into the matrix should lead to some increase in the driving force behind the molybdenum precipitation. Thus the amount of molybdenum in the matrix should continue to decrease upon further aging. Because the titanium is almost completely depleted and the precipitates likely has a nominal ratio of titanium to molybdenum, further incorporation of molybdenum into precipitates should mainly grow the μ-phase.

4.5 Precipitation Process

The results presented previously indicates that the precipitation starts with the clustering of titanium and nickel, followed by creation of $Ni_3(Ti, Mo)$-spheres, indi-

Table 4.4: Elemental composition of the matrix and identified precipitates in the sample aged 180 min

Conc. at.%	Fe	Ni	Co	Mo	Ti
Matrix	79.4	10.3	9.60	0.672	0.0153
$Ni_3(Ti, Mo)$	15.9	55.3	1.89	2.61	23.9
$Ni_3(Mo, Ti)$	27.1	51.8	4.73	11.6	6.93
μ-Fe_7Mo_6	41.7	17.3	4.48	39.4	0.150

cated by the as-built sample microstructure. The clustering seems to preferentially take place in titanium-richer grains and in these close to grain boundaries as this is what was found in the specimens analysed. The precipitate properties over time, a summary given in table 4.5, show that while the number density slightly decreases on average on aging, the volume fraction increases with time, indicating growth of some precipitates at the expense of others. The mean and median radii show a slight decrease from 15 minutes of aging to 30 minutes of aging, but then an increase after 180 min. This can be attributed to the growth of μ-type precipitates depleting some $Ni_3(Mo, Ti)$-rods of molybdenum, allowing their transformation into larger $Ni_3(Ti, Mo)$-particles with a more rod-like appearance. The general trend is however for the precipitates to slowly grow in size while becoming fewer.

Table 4.5: Precipitate properties of the $Ni_3(Ti, Mo)$-particles for the different times and samples. The two different specimens of the 30 min sample are shown separately.

Specimen	as-built	15 min	30 min 1	30 min 2	180 min
Number density ($10^{23}\,m^{-3}$)	3.7	5.0	1.0	5.8	3.4
Volume fraction (%)	0.1	0.32	1.8	0.06	0.86
Mean radius (nm)		1.21	1.02	1.13	1.51
Median radius (nm)		1.16	1.07	1.06	1.27

The $Ni_3(Mo, Ti)$ rods seem to have a different beginning than the $Ni_3(Ti, Mo)$-spheres. In the as-built material no clustering of molybdenum was evident. Examination of the precipitate in samples aged 15 min show a relatively long but narrow structure. The rod-like structure of these precipitates could be a consequence of the way they are formed. It could be that they form from dislocations in the lattice as the large radius of the molybdenum atoms could lower the lattice strain there, giving a preferential diffusion to these sites. This is further supported by the number of such rods cutting through a two dimensional plane in the volume, at about $1 \times 10^{11}\,cm^{-2}$ to $4 \times 10^{11}\,cm^{-2}$ it is comparable to the dislocation density of the martensite in a similar steel [22]. One of the detected rods in a 30 min-specimen showed a different composition. Perhaps this composition is an early stage of the formation of the rods, before significant amounts of nickel can be absorbed. It was found attached in one end to a $Ni_3(Ti, Mo)$-sphere and this could have interfered with its growth into a $Ni_3(Mo, Ti)$ form.

The size evolution of these precipitates show a tendency towards an increase in size with aging, as summarized in table 4.6, while the number of precipitates seem relatively fixed. The large distances between the rods and the availability

Table 4.6: Precipitate properties of the $Ni_3(Mo, Ti)$-rods and plates for the different times and samples. The more precipitate dense region of the 15 min specimen is marked by a 2, and the more common distribution with a 1. The two different specimens of the 30 min sample are also shown separately.

Specimen	15 min 1	15 min 2	30 min 1	30 min 2	180 min
Number density ($10^{23}\,m^{-3}$)	1.7	2.7	1.4	1.1	2.6
Volume fraction (%)	1.9	6.5	2.5	5.4	3.6
Thickness (nm)	4-6	4-6	4-6	5-6	5-7
Width (nm)	4-9	6-10	6-13	5-12	6-15

of molybdenum in the matrix could be a reason why they seemingly grow without interference with each other. As titanium also is an important constituent and is not available in the matrix their growth should be stunted, but as they are surrounded by $Ni_3(Ti, Mo)$ particles growth at the expense of these would be possible. The reason for molybdenum to grow these precipitates is that the increased cobalt content of the matrix decreases the solubility of molybdenum to near zero. Another pathway for the molybdenum to be rejected from the matrix, is the μ-type precipitates.

As the μ-precipitates require a very high amount of molybdenum their formation from the matrix would require a high degree of clustering of molybdenum. As no clustering before aging was detected this neatly explains why there is such a lack of μ-particles in the sample aged 15 min, as is shown in table 4.7. The μ-precipitates seem to instead form through transformation from the more molybdenum rich rods. As the aging progresses the volume fraction of the μ phase grow a lot. The same is true for the number density, likely a consequence of a minimum size/composition required for the rods to nucleate the μ-phase. When the μ phase has nucleated it can likely absorb molybdenum from both the matrix and nearby $Ni_3(Mo, Ti)$ rods to grow rather quickly.

Table 4.7: Precipitate properties of the μ-Fe_7Mo_6-precipitates for the different times. Here the Mo > Ni isosurface was used for a more consistent comparison. Note that local magnification makes the measured diameter larger than 2 times the radius calculated with the lattice size method.

Sample	15 min	30 min	180 min
Number density ($10^{22}\,m^{-3}$)	1.9	1.9	10
Volume fraction (%)	0.02	0.18	0.86
Measured diameter (nm)	2-4	2-8	8-13
Mean radius (nm)	0.835	1.05	2.11
Median radius (nm)	0.741	0.840	1.82

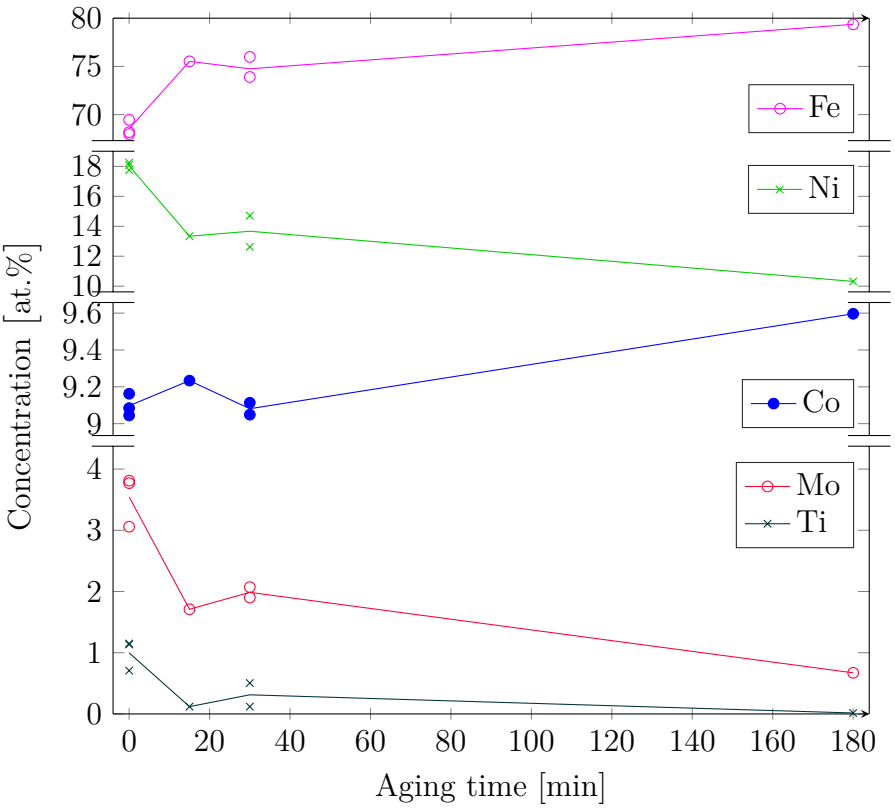

Figure 4.15: The composition measured in the matrix at the different aging stages. Note that the lines are simple averages of the measured compositions in the areas analysed.

The matrix composition in the steel over time is presented in fig. 4.15. Of note here is that the relatively small volumes of the 30 minute reconstructions could be unrepresentative of the sample as a whole. It is clear that the matrix depletes of solute very quickly with the majority of change in Ni, Mo and Ti occurring during the first 15 minutes.

The change in cobalt content seems to be slower, with most change occurring after the 30 minute mark. An explanation for this could be that the diffusion of cobalt out of the precipitates may be relatively slow and a much longer time is needed for it to be rejected. Another explanation could be if the μ phase allows a faster transport of cobalt, perhaps through a larger incompatibility with its own lattice, as it is not present in large volumes until later aging stages. This would, however, not explain why the cobalt content was consistently lower in $Ni_3(Ti, Mo)$ compared to the other phases for all aging times. In light of this it would be more likely that it is the transformation of $Ni_3(Mo, Ti)$ to $Ni_3(Ti, Mo)$ that was observed.

In addition to the previously described precipitates, there were also spherical oxide and nitride particles present in some of the specimen volumes. Both of these had distinct peaks of titanium oxide or nitride. Visible in the mass spectrum from the peaks at 31 and 32 being surrounded by 2 smaller peaks on each side with ratios close to that of titanium isotopes. The concentrations, presented in table 4.8, show that most of the discovered precipitates are titanium/aluminium oxides. There is

one, however, that is a clear nitride. It has a titanium to nitrogen ratio of about 1.7, coming quite close to the Ti_2N composition reported by Zhu *et al.* [17]. These oxides and nitride particles could contribute to or decrease the strength of the steel, they do however seem to remain relatively constant in size and composition upon aging. They should therefore not contribute to a significant portion of the strength gained during aging.

Table 4.8: The main composition of various oxide and nitride particles. The remainder of the composition is mostly iron or nickel in ratios close to the matrix.

Conc. at.%	O	Ti	Al	N
3h	35.1	29.5	10.5	not detected
3h	32.4	19.2	25.1	not detected
as-built	29.9	20.2	19.2	not detected
as-built	11.4	47.8	not detected	28.4

5

Conclusion

The precipitates detected at the various aging times give useful clues to the mechanics of the precipitation process. Thanks to the excellent resolution of the atom probe, detection of very small particles even in the as-built state was possible.

Already in the as-built state, initial stages of precipitation of $Ni_3(Ti, Mo)$ was discovered, showing that the laser powder bed fusion process had resulted in some intrinsic heat treatment of the material. In addition to these particles, the titanium and nickel in the as-built sample showed some clustering, supporting the finding that it was the $Ni_3(Ti, Mo)$ and not the $Ni_3(Mo, Ti)$ phase that precipitated first.

After 15 minutes of aging the sample showed a much more developed microstructure with clear rod-like $Ni_3(Mo, Ti)$ precipitates in addition to a large number of spherical $Ni_3(Ti, Mo)$ particles. The rods were around 5 nm thick and many were more than 50 nm long. These could likely have the same type of lattice as the η-$Ni_3(Ti, Al)$-rods described for a maraging stainless steel. A proposed mechanism for their creation is molybdenum clustering at dislocations, to further investigate this, samples aged for even shorter times than 15 minutes would have to be examined. At the ends of some of these rods and where they connected with each other a formation of the Fe_7Mo_6 μ-phase was observed. They had barely started developing at this time with a volume fraction of 0.02 %.

With further aging to 30 min there was a slight coarsening of the $Ni_3(Mo, Ti)$-rods and the $Ni_3(Ti, Mo)$-spheres. There was however no successful runs with much data collection for this state, making the analysis difficult and possibly unrepresentative. The analysis of the 30 min sample could be extended with additional measurements to determine if the volumes analysed were representative. The biggest difference from the 15 minute condition was in the size of the μ-precipitates, them now making up about 0.18 % of the volume, and in that the rods were now also found as plates with a thickness to width ratio of up to 1:3.

Upon aging for 180 minutes, significant precipitation had occurred. In the matrix almost no titanium remained t a concentration of 0.02 at.% and very little molybdenum, 0.67 at.%, was present. The iron and cobalt had been left behind in the matrix when precipitates formed from the other solutes. An increased number and size of μ-precipitates were detected, all in contact with $Ni_3(Mo, Ti)$-rods indicating that they nucleate somewhere within or on an interface of these. The $Ni_3(Ti, Mo)$-phase could now be found as small rod-like areas connected with the larger $Ni_3(Mo, Ti)$-rods. This is likely caused by the $Ni_3(Mo, Ti)$-rods depleting in molybdenum when the μ-phase grows. The mode of the size distribution of the $Ni_3(Ti, Mo)$-spheres had diminished somewhat, indicating that they were being consumed by other precipitates during aging.

Because the 180 minute aging time is recommended for optimal strength according to previous studies, it is likely that the coarsening of the $Ni_3(Mo, Ti)$-rods is the main strengthening mechanism. Further aging would likely start consumption of these to grow the μ-phase that largely contributes to embrittlement, but further studies on the continued evolution would be required to determine what actually happens.

Bibliography

1. Xiong, Z., Timokhina, I. & Pereloma, E. Clustering, nano-scale precipitation and strengthening of steels. *Progress in Materials Science,* 100764 (2020).
2. Bajaj, P., Hariharan, A., Kini, A., Kürnsteiner, P., Raabe, D. & Jägle, E. A. Steels in additive manufacturing: A review of their microstructure and properties. *Materials Science and Engineering: A* **772,** 138633 (2020).
3. Dos Reis, A. G., Reis, D. A. P., Abdalla, A. J. & Otubo, J. High-temperature creep resistance and effects on the austenite reversion and precipitation of 18 Ni (300) maraging steel. *Materials Characterization* **107,** 350–357 (2015).
4. Sovacool, B. K. The precarious political economy of cobalt: Balancing prosperity, poverty, and brutality in artisanal and industrial mining in the Democratic Republic of the Congo. *The Extractive Industries and Society* **6,** 915–939 (2019).
5. Norgate, T., Jahanshahi, S. & Rankin, W. Assessing the environmental impact of metal production processes. *Journal of Cleaner Production* **15,** 838–848 (2007).
6. Kittel, C. & McEuen, P. *Introduction to solid state physics* (Wiley New York, 1996).
7. Porter, D. A. & Easterling, K. E. *Phase transformations in metals and alloys* (Van Nostrand Reinhold (international) Co.Ltd, 1988).
8. Sha, W., Leitner, H., Guo, Z. & Xu, W. in *Phase transformations in steels* 332–362 (Elsevier, 2012).
9. Conde, F. F., Escobar, J. D., Oliveira, J. P., Jardini, A., Bose Filho, W. & Avila, J. Austenite reversion kinetics and stability during tempering of an additively manufactured maraging 300 steel. *Additive Manufacturing* **29,** 100804 (2019).
10. *Amperprint® 1556 18Ni300* Höganäs AB (2021). `https://www.hoganas.com/en/powder-technologies/products/amperprint/amperprint-1556-fenicomo-18ni300-15-45/`.
11. Bodziak, S. *et al.* Precipitation in 300 grade maraging steel built by selective laser melting: Aging at 510 °C for 2 h. *Materials Characterization* **151,** 73–83 (2019).
12. Allam, T., Pradeep, K., Köhnen, P., Marshal, A., Schleifenbaum, J. & Haase, C. Tailoring the nanostructure of laser powder bed fusion additively manufactured maraging steel. *Additive Manufacturing* **36,** 101561 (2020).
13. Król, M., Snopiński, P. & Czech, A. The phase transitions in selective laser-melted 18-NI (300-grade) maraging steel. *Journal of Thermal Analysis and Calorimetry,* 1–8 (2020).

14. Yao, Y., Huang, Y., Chen, B., Tan, C., Su, Y. & Feng, J. Influence of processing parameters and heat treatment on the mechanical properties of 18Ni300 manufactured by laser based directed energy deposition. *Optics & Laser Technology* **105,** 171–179 (2018).
15. Bai, Y., Yang, Y., Wang, D. & Zhang, M. Influence mechanism of parameters process and mechanical properties evolution mechanism of maraging steel 300 by selective laser melting. *Materials Science and Engineering: A* **703,** 116–123 (2017).
16. Dehgahi, S., Ghoncheh, M., Hadadzadeh, A., Sanjari, M., Amirkhiz, B. S. & Mohammadi, M. The role of titanium on the microstructure and mechanical properties of additively manufactured C300 maraging steels. *Materials & Design* **194,** 108965 (2020).
17. Zhu, H., Zhang, J., Hu, J., Ouyang, M. & Qiu, C. Effects of aging time on the microstructure and mechanical properties of laser-cladded 18Ni300 maraging steel. *Journal of Materials Science* **56,** 8835–8847 (2021).
18. Jägle, E. A., Choi, P.-P., Van Humbeeck, J. & Raabe, D. Precipitation and austenite reversion behavior of a maraging steel produced by selective laser melting. *Journal of Materials Research* **29,** 2072–2079 (2014).
19. Gault, B., Moody, M. P., Cairney, J. M. & Ringer, S. P. *Atom probe microscopy* (Springer Science & Business Media, 2012).
20. Miller, M. K. & Forbes, R. G. Atom-Probe Tomography: The Local Electrode Atom Probe (2014).
21. Thuvander, M., Andersson, M. & Stiller, K. Multiple Influences of Molybdenum on the Precipitation Process in a Martensitic PH Stainless Steel. *Metals* **9,** 1118 (2019).
22. Macek, K. *et al.* Austenite content and dislocation density in electron-beam welds of a stainless maraging steel. *Materials Science and Engineering: A* **208,** 131–138 (1996).

DEPARTMENT OF PHYSICS
CHALMERS UNIVERSITY OF TECHNOLOGY
Gothenburg, Sweden 2021
www.chalmers.se

CHALMERS
UNIVERSITY OF TECHNOLOGY